Author Manuscript
Author Manuscript
Author Manuscript
Author Manuscript

HHS Public Access
Author manuscript
Nature. Author manuscript; available in PMC 2018 June 06.

Published in final edited form as:
Nature. 2017 December 14; 552(7684): 187–193. doi:10.1038/nature25143.

Enhancing mitochondrial proteostasis reduces amyloid-β proteotoxicity

Vincenzo Sorrentino[1], **Mario Romani**[1,*], **Laurent Mouchiroud**[1,*], **John S. Beck**[2], **Hongbo Zhang**[1], **Davide D'Amico**[1], **Norman Moullan**[1], **Francesca Potenza**[1], **Adrien W. Schmid**[3], **Solène Rietsch**[1], **Scott E. Counts**[2], and **Johan Auwerx**[1]

[1]Laboratory for Integrative and Systems Physiology, Institute of Bioengineering, Ecole Polytechnique Fédérale de Lausanne, CH-1015 Lausanne, Switzerland [2]Department of Translational Science and Molecular Medicine, Department of Family Medicine, Michigan State University, Grand Rapids, MI 49503, USA [3]Proteomics Core Facility, Ecole Polytechnique Fédérale de Lausanne, CH-1015 Lausanne, Switzerland

Abstract

Alzheimer's disease (AD) is a common and devastating disease characterized by the aggregation of amyloid-β peptide (Aβ), yet we know relatively little about the underlying molecular mechanisms or how to treat AD patients. Here, we provide bioinformatic and experimental evidence of a conserved mitochondrial stress response signature present in Aβ proteotoxic diseases in human, mouse and *C. elegans*, and which involves the UPR^{mt} and mitophagy pathways. Using the worm model of Aβ proteotoxicity, GMC101, we recapitulated mitochondrial features and confirmed the induction of this mitochondrial stress response as key to maintain mitochondrial proteostasis and health. Importantly, boosting mitochondrial proteostasis by pharmacologically and genetically targeting mitochondrial translation and mitophagy increases fitness and lifespan of GMC101 worms and reduces amyloid aggregation in cells, worms, and in AD transgenic mice. Our data support the relevance of enhancing mitochondrial proteostasis to delay Aβ proteotoxic diseases, such as AD.

Aging is often accompanied by the onset of proteotoxic degenerative diseases, characterized by the accumulation of unfolded and aggregated proteins. Amyloid diseases are proteotoxic disorders, which can affect the nervous system, like in the case of Alzheimer's (AD), the

Users may view, print, copy, and download text and data-mine the content in such documents, for the purposes of academic research, subject always to the full Conditions of use: http://www.nature.com/authors/editorial_policies/license.html#termsReprints and permissions information is available at www.nature.com/reprints.

Correspondence and requests for materials should be addressed to J.A. (admin.auwerx@epfl.ch).
*These authors contributed equally to this work

Online Content Methods, along with any additional Extended Data display items, are available in the online version of the paper; references unique to these sections appear only in the online paper.

Supplementary Information is linked to the online version of the paper at www.nature.com/nature.

Author contributions V.S. and J.A. conceived and designed the project. V.S., L.M., M.R., J.S.B., H.Z., D.D., F.P., N.M., A.S., S.R., and S.E.C. performed the experiments. V.S., M.R., and L.M. independently replicated worm experiments on figures 2–4. V.S., L.M. and J.A. wrote the manuscript.

The authors declare no competing financial interests.

Author Manuscript Author Manuscript Author Manuscript Author Manuscript

most common form of dementia[1], but also other organs, as exemplified by amyloidosis-associated kidney disease[2] and inclusion body myositis (IBM)[3]. To date, no efficient therapy is available for AD[4], a disease with a strong component of amyloid-β (Aβ) aggregation[1]. Clinical trials for AD focused primarily on counteracting Aβ aggregation in the brain, considered the key pathogenic mechanism[5]. However, AD is a complex multifactorial disease[6] and mitochondrial dysfunction emerged as a common pathological hallmark[7]. Mitochondrial abnormalities in AD include decreased mitochondrial respiration and activity and alterations in mitochondrial morphology[7]; however, the relevance of other aspects of mitochondrial homeostasis, such as mitochondrial proteostasis, to the pathogenesis of AD is still largely unknown.

Mitochondrial function pathways are perturbed in AD

We investigated brain expression datasets from AD patients (GN327, GN328 and GN314) archived in GeneNetwork (www.genenetwork.org) to define the mitochondrial signature associated with the disease. Gene Set Enrichment Analysis (GSEA) of datasets from healthy *versus* AD individuals in prefrontal, primary visual cortex and whole brain showed that downregulation of mitochondrial oxidative phosphorylation (Oxphos) and perturbation of mitochondrial import pathways were hallmarks of AD (Fig. 1a, Extended Data Fig. 1a,b,c,e,f and Supplementary Table 1–4). As these processes are linked with, and affect mitochondrial proteostasis[8], we used comprehensive gene sets for two major mitochondrial quality control pathways, the mitochondrial unfolded protein response (UPR^{mt}) and mitophagy, to evaluate whether their expression is co-regulated in AD patients (Supplementary Table 5). Whereas we observed a tight correlation between genes typifying UPR^{mt} and mitophagy in all brain datasets investigated (Fig. 1b and Extended Data Fig. 1d,g), other stress pathways, such as the ER stress (UPR^{er}) and heat shock response (HSR) were co-regulated to a lower degree (Fig. 1b and Extended Data Fig. 1d,g).

Evidence for a mitochondrial stress signature in AD

We then measured UPR^{mt}, mitophagy and Oxphos transcripts in human cortex. Previously, we reported that several UPR^{mt} genes were up-regulated during frank familial or sporadic AD[9]. Here, we extended that analysis and observed that, compared to subjects with no cognitive impairment (NCI), several UPR^{mt} and mitophagy transcripts were also up-regulated in patients with mild cognitive impairment (MCI), a putative prodromal AD stage[10], and in mild/moderate AD (Fig. 1c and Supplementary Table 6), whereas Oxphos genes were down-regulated, consistent with our GSEA. The induction of this mitochondrial stress response was also observed at the protein level in MCI and AD subjects (Fig. 1d). The occurrence of this perturbation already in MCI suggests that mitochondrial dysfunction contributes to neuron and synapse loss, and that mitochondrial stress pathways may be activated as a protective response during disease progression[10]. We also analyzed cortex samples of wild-type (WT) and 3xTgAD mice[11] (Extended Data Fig. 2a) at 6 and 9 months of age. Both mitochondrial quality control and Oxphos genes were induced in AD mice (Fig. 1e and Extended Data Fig. 2b), although to a different extent over time. In fact, pairing WT and AD animals at these two times indicated a marked attenuation of this stress signature during disease progression (Extended Data Fig. 2d–f). Immunoblotting of total lysates from

Author Manuscript Author Manuscript Author Manuscript Author Manuscript

the cortex of WT and 3xTgAD mice showed the induction of PINK1, LONP1 and LC3 at both time points (Fig. 1f and Extended Data Fig. 2c). Additional analysis of the 9-month old animals also indicated a reduction in VDAC, a marked increase in P62 phosphorylation (Fig. 1g), and reduced citrate synthase (CS) activity (Extended Data Fig. 2g) in AD mice, indicative of autophagy and mitophagy. PINK1 and LC3-I were also increased in mitochondrial extracts from cortex samples of the AD mice (Fig. 1g), confirming that these proteins are recruited to the mitochondria to promote mitophagy, as supported by the augmented ubiquitylation of mitochondrial proteins (Fig. 1g). For simplicity, we abbreviate the comprehensive mitochondrial stress footprint analyzed herein as Mitochondrial Stress Response (MSR).

Identification of a cross-species MSR signature

The functional impact of changes in mitochondrial homeostasis during disease and aging in mammals can be rather faithfully translated in the nematode *Caenorhabditis elegans*[12]. Worm models of Aβ aggregation have been extensively used to study the basic consequences of proteotoxic stress on conserved biological pathways between worms and mammals[13,14]. We took advantage of the GMC101 worm model of Aβ proteotoxicity. GMC101 worms constantly express the human Aβ isoform 1–42 in muscle cells, but adults only develop age-progressive paralysis and amyloid deposition in the body wall muscle after a temperature shift from 20 to 25°C[15], while the control strain CL2122 does not express the Aβ peptide (Extended Data Fig. 3a).

Transcripts of the worm orthologs of the MSR were induced in adult GMC101 worms compared to CL2122 following the temperature shift (Fig. 2a), while only partially perturbed at 20°C (Extended Data Fig. 3b). Basal and maximal respiratory capacity were decreased in GMC101 (Fig. 2b and Extended Data Fig. 3c), in contrast with the increased Oxphos transcript levels (Fig. 2a), suggesting a compensatory induction to ensure respiration. Mitochondrial content was lower in GMC101, as shown by decreased Oxphos proteins, mt/nDNA ratio and CS activity (Fig. 2c and Extended Data Fig. 3d–e). Importantly, GMC101 fitness, measured as spontaneous movement[16], was robustly reduced relative to CL2122 in line with the muscle disorganization and alteration of the mitochondrial network in the body wall muscle (Extended Data Fig. 3f,g). These data highlight the cross-species conservation of the MSR, and make GMC101 an excellent proxy to characterize the mitochondrial dysfunction and phenotypic impact observed in Aβ diseases in mammals.

Mitochondrial homeostasis counters Aβ proteotoxicity

The control of mitochondrial function and UPR^{mt} during stress in the worm is largely attributable to the activating transcription factor associated with stress, *atfs-1*[17,18]. Depletion of *atfs-1* by RNAi feeding of the GMC101 worms, but not CL2122, caused a severe developmental delay even in absence of the “disease-inducing” temperature shift (Extended Data Fig. 3h), phenocopying mitochondrial respiration mutants that rely on *atfs-1* for survival and adaption[18]. Comparative analysis of transcripts involved in cytosolic and nuclear adaptation pathways, such as UPR^{er}, HSR, and *daf-16,* showed also a mild induction of the UPR^{er} and a striking upregulation of the HSR in GMC101 (Extended Data Fig. 3i), in

Author Manuscript Author Manuscript Author Manuscript Author Manuscript

line with the role of HSR as a primary defense against proteotoxic stress in worm[19]. We therefore evaluated the effect of RNAis targeting key regulators of these pathways, *hsf-1* and *xbp-1*, on the development of GMC101. Only *atfs-1* RNAi again led to extreme developmental delays, while no alterations were observed with all these RNAis in CL2122 (Extended Data Fig. 3j).

Importantly, basal and maximal respiration in adult GMC101 was significantly impaired upon *atfs-1* silencing, while only maximal respiration was partially affected in CL2122 (Fig. 2d). In addition, *atfs-1* RNAi exacerbated aggregation (Fig. 2e and Extended Data Fig. 3k) and paralysis (Fig. 2f) in GMC101, while CL2122's mobility was unaffected (Extended Data Fig. 3l). Furthermore, *atfs-1* knockdown in GMC101 prominently repressed the MSR signature, including mitophagy effectors (Fig. 2g), whereas in CL2122, *pdr-1*, *dct-1* and Oxphos transcripts were even induced, in spite of *atfs-1* silencing in both strains (Extended Data Fig. 3m,n).

Given the induction of the HSR in the GMC101, we tested whether *hsf-1* repression would impact on fitness. Interestingly, while *atfs-1* knockdown only paralyzed GMC101, silencing of *hsf-1* reduced mobility in both CL2122 and wild-type N2 strains when incubated at 25°C (Extended Data Fig. 3o), reflecting a general effect of *hsf-1* on homeostasis independent of the strain. Worm mobility was similarly impaired in GMC101, but not in CL2122, following silencing of *atfs-1* with an alternative RNAi we generated (*atfs-1 #2*) (Extended Data Fig. 3p,q and Supplementary Table 13), confirming a specific role of *atfs-1* in ensuring organismal homeostasis in GMC101. Furthermore, silencing of *ubl-5*, another positive regulator of the UPR^{mt}[20], also delayed development and decreased health- and lifespan specifically in GMC101 (Extended Data Fig. 4a–c). Intriguingly, *atfs-1* silencing led to further upregulation of the HSR in GMC101 and to its induction in CL2122 (Extended Data Fig. 4d,e), while repressing the MSR specifically in GMC101 (Fig. 2g and Extended Data Fig 3n).

Conversely, to enhance *atfs-1* function, we generated two GMC101-derived strains, AUW9 and AUW10, and one CL2122 line (AUW11), overexpressing *atfs-1* (Supplementary Table 12,13). This resulted in the induction of the UPR^{mt} (Extended Data Fig. 4f), a significant increase in fitness, and a discrete decrease in paralysis and death scores in the GMC101-derived strains AUW9 and AUW10 (Fig. 2h and Extended Data Fig. 4g,h), while no changes were observed in AUW11 (Extended Data Fig. 4g). As an alternative approach to increase mitochondrial stress response, we crossed GMC101 with two long-lived mitochondrial mutants, *i.e. clk-1*[21] and *nuo-6*[22] (Supplementary Table 12,13). Consistently, GMC101 with a mutation in these mitochondrial genes (AUW12 and AUW13) manifested intermediate phenotypes between GMC101 and their mitochondrial mutant counterpart, with enhanced healthspan and lifespan (Extended Data Fig. 4i–l).

Altogether, this indicates that *atfs-1* and the MSR induction ensure proteostasis and survival in this worm model of Aβ aggregation, and that mitochondria play an active, rather than passive, role during Aβ proteotoxic stress. This prompted us to investigate the potential of boosting mitochondrial proteostasis to curb the progression of this deleterious phenotype.

Author Manuscript Author Manuscript Author Manuscript Author Manuscript

Reducing mitochondrial translation lowers Aβ proteotoxicity

Given the tight link between the UPR^{mt} and AD observed above, we investigated the effects of two established strategies to induce the UPR^{mt} in *C. elegans*; genetically, by silencing the expression of the mitochondrial ribosomal protein *mrps-5*[23], and pharmacologically, by using the mitochondrial translation inhibitor doxycycline (dox)[23,24]. Both interventions, which favor worm health and lifespan[23], markedly induced transcripts of UPR^{mt}, mitophagy and respiration genes in GMC101 (Fig. 3a,b), without causing major development and growth delays (Extended Data Fig. 5a). Dox similarly induced these pathways in CL2122 (Extended Data Fig. 5b). No perturbations of UPR^{er} and HSR in GMC101 treated with dox or *mrps-5* RNAi were observed (Extended Data Fig. 5c,d), while one *daf-16* target, mitochondrial superoxide dismutase *sod-3,* was induced (Extended Data Fig. 5c,d). The transcriptional induction of the MSR impacted beneficially on fitness and lifespan of GMC101 (Fig. 3c–e). Furthermore, Aβ aggregation was reduced by *mrps-5* RNAi and dox (Fig. 3f and Extended Data Fig. 5e). Of essence, the improvement in motility and Aβ clearance in GMC101 required *atfs-1* (Fig. 3g,h), proving the vital contribution of the UPR^{mt} to the phenotypic improvements. Respirometry on GMC101 worms fed with *mrps-5* RNAi at D3 and D6 of adulthood (Extended Data Fig. 5f), showed that *mrps-5* knockdown prevented the decrease in respiration upon aging, suggesting a stabilization of mitochondrial function following the MSR-dependent improvement of proteostasis.

We then extended our investigation to a mammalian SY5Y neuroblastoma cell line expressing the APP Swedish K670N/M671L mutation (APP_{Swe})[25]. Dox markedly reduced intracellular Aβ deposits, as shown with an Aβ1-42-specific antibody (Fig. 3k and Extended Data Fig. 5g). This improvement was linked to a mito-nuclear protein imbalance and the induction of components of the MSR (Extended Data Fig. 5h,i). These results add to observations of *in vitro*[26] and *in vivo* studies in AD flies[27] and patients[28], which suggested that dox treatment may ameliorate AD and Aβ aggregation. Recently, the regulation of the mitochondrial stress responses in mammals, including dox-dependent mitochondrial stress, was shown to rely on the activation of the integrated stress response (ISR) and on the transcription factor ATF4[29–31]. Pretreating cells with ISRIB, a global ISR inhibitor[32], prevented amyloid clearance by dox and hampered the dox-mediated induction of canonical ATF4 target genes, such as *CHOP* and *CHAC1*[29] (Fig. 3k and Extended Data Fig. 5g,j). This suggests the involvement of the ISR in resolving Aβ proteotoxic stress in mammalian cells.

Given the induction of mitophagy in 3xTgAD mice, human AD patients and in GMC101 worms, and its further increase upon *mrps-5* RNAi and dox treatments, we also tested the contribution of mitophagy to the homeostasis of GMC101. To achieve this, we silenced by RNAi *dct-1*, an evolutionarily conserved regulator of mitophagy[33]. *dct-1* RNAi reduced GMC101's health- and life-span already in basal conditions (Extended Data Fig. 5k–m). Furthermore, it blunted the positive effects of *mrps-5* RNAi and dox on health- and lifespan (Fig. 3i and Extended Data Fig. 5l,m) and proteostasis (Fig. 3j). Conversely, *dct-1* knockdown in CL2122 affected their movement only during aging (Extended Data Fig. 5n,o), stressing the relevance of mitophagy in aging. Altogether, these data show that mitophagy, in addition to UPR^{mt}, is also induced and required for the survival of GMC101 worms and for the beneficial effects of the described interventions.

Author Manuscript Author Manuscript Author Manuscript Author Manuscript

NAD+ boosters attenuate Aβ proteotoxicity

The UPR^{mt} and mitophagy pathways are also potently induced in worms and in various mammalian tissues by NAD$^+$-boosting compounds, such as nicotinamide riboside (NR), and Olaparib (AZD2281 or AZD)[34–37]. Similarly to dox and *mrps-5* RNAi, treatment of GMC101 with NR and AZD induced the MSR (Fig. 4a,b), and improved health- and lifespan (Fig. 4c–d and Extended Data Fig. 6a). The NR- and AZD-mediated induction of the MSR was also observed in CL2122 (Extended Data Fig. 6b,c), but, these treatments only improved CL2122 fitness during aging (Extended Data Fig. 6d,e), similarly to what previously was shown in N2 worms[34]. In addition, treatment of GMC101 with NR and AZD reduced proteotoxic stress (Fig. 4e). Importantly, the NR-mediated phenotypic and proteostasis benefits required *atfs-1* (Fig. 4f–h, Extended Data Fig. 6f) and *dct-1* (Fig. 4i–k, Extended Data Fig. 6g). NR has been shown to increase sirtuin activity, and activate the FOXO/*daf-16* signaling in mammals and *C. elegans*[34]. Therefore, we evaluated the effect of *daf-16* and *sir-2.1* silencing on development, healthspan and NR-dependent benefits of GMC101. While *sir-2.1* knockdown did not delay growth of GMC101 or its control (Extended Data Fig. 6h), it increased paralysis and death in the GMC101 similarly to *dct-1* and *atfs-1* RNAis (Extended Data Fig. 6i,k). However, NR still significantly rescued health- and life-span of GMC101 fed with *sir-2.1*, showing that the effects of NR rely mostly on *atfs-1* and *dct-1* (Extended Data Fig. 6i,k). Instead, feeding GMC101 with *daf-16* RNAi did not result in major phenotypic changes (Extended Data Fig. 6h,j,k). Furthermore, NR did not affect the expression of *daf-16* and its targets (Extended Data Fig. 6l). NR and AZD had only a minimal impact on UPR^{er} and HSR in GMC101, with the induction of *hsp-16.41* and *hsp-16.48/49* (Extended Data Fig. 6l,m). These results indicate that in the GMC101 model, the main mode of action of NAD$^+$ boosting involves the induction of the MSR.

We also assessed the effect of NR in the Aβ-expressing neuronal cells and consistent with the data in *C. elegans*, we observed a remarkable reduction of the intracellular Aβ deposits with NR (Fig. 4l and Extended Data Fig. 6n), accompanied by increased Oxphos protein (Extended Data Fig. 5h) and MSR transcript levels (Extended Data Fig. 6o).

NR reduces Aβ levels in AD transgenic mice

We have previously shown that NR exerts beneficial effects on health- and lifespan[34,36], but whether it also improves mitochondrial function and proteostasis *in vivo* in a mouse model of Aβ proteotoxicity is so far unknown. We hence treated *APP/PSEN1* AD mice with NR and assessed the levels of Aβ plaques in brain with Thioflavin S, as well as mitochondrial Oxphos and MSR transcript and protein expression. In agreement with the effects observed in cells and worms, NR robustly reduced Aβ deposits in cortex tissues of the AD mice (Fig. 5a), and induced the MSR mRNA signature (Fig. 5b) and Oxphos protein levels (Fig. 5c). NR also enhanced context-dependent memory in the *APP/PSEN1* AD mice, which was impaired compared to WT animals, as assessed by contextual fear conditioning[38] (Fig. 5d), suggesting a potential positive impact on cognitive function. We hence propose that restoring or boosting mitochondrial function and proteostasis induces a conserved repair mechanism, from worm to mouse that leads to decreased Aβ proteotoxicity and improves health- and lifespan.

Author Manuscript Author Manuscript Author Manuscript Author Manuscript

Discussion

Proteotoxic stress in Aβ diseases, such as AD, is associated with mitochondrial dysfunction, and reduced Oxphos activity has been considered one of the major hallmarks of these diseases. Here, we identify a cross-species mitochondrial stress response signature that implicates mitochondrial proteostasis as a key mechanism in the response to Aβ proteotoxic stress. Most importantly, we show that Aβ accumulation induces both the UPR^{mt} and mitophagy in a strikingly conserved manner from *C. elegans* to humans. Currently, the molecular mechanism driving this induction is still unclear. Based on our results, we speculate that it must involve the alteration of a basic, conserved functional process, such as for instance mitochondrial import, which is linked to the activation of the UPR^{mt}[18], is perturbed during Aβ proteotoxic stress[39] and is downregulated in AD patients in our analyses. Our work also provides solid evidence that mitochondria play an active role in the pathogenesis of Aβ diseases, as reducing mitochondrial homeostasis via *atfs-1* depletion in GMC101 worms aggravates the hallmarks of the disease (model in Extended Data Fig. 7); conversely, boosting mitochondrial proteostasis by increasing the UPR^{mt} and mitophagy decreases protein aggregation, restores worm fitness and delays disease progression, ultimately translating in increased lifespan. Similarly, in mammals we show that dox and NR decrease Aβ accumulation in a neuronal cell model and that NR treatment reduces amyloid plaque formation in brain and improves contextual memory in *APP/PSEN1* AD mice. These findings indicate that boosting mitochondrial function and proteostasis may decrease the formation of detrimental protein aggregates in the context of proteotoxic disease, typified by reduced mitochondrial activity and loss of proteostasis. Together with initial evidence suggesting potential benefits of targeting dysfunctional mitochondria in AD[26–28,40,41] and in view of recent findings linking mitochondrial stress to the induction of cytosolic proteostasis mechanisms[42–45], our data support the concept that enhancing mitochondrial proteostasis may hold promise to manage pervasive Aβ proteopathies, such as AD.

Methods

Animal experiments

3xTg AD mice, bearing human mutant APPswe, PS1M146V, and TauP301L transgenes[11], and wild-type, hybrid 129/C57BL6 mouse littermates were transcardially perfused with saline at 6 and 9 months of age (n = 6/group) and brains from each group were hemisected. One hemisphere was immersion-fixed in 4% paraformaldehyde/0.1% glutaraldehyde for 24 hours and stored in cryoprotectant. From the other hemisphere, hippocampus, frontoparietal cortex, and cerebellum were rapidly dissected and snap-frozen.

APP/PSEN1 mice (Tg(APPswe,PSEN1dE9)85Dbo/Mmjax) were purchased from JAX. *APP/PSEN1* mice were fed NR pellets (400 mg/kg/day) for 10 weeks, starting at the age of 4 months. The pellets were prepared by mixing powdered chow diet (2016S, Harlan Laboratories) with water or with NR dissolved in water. Pellets were dried under a laminar flow hood for 48 hours. Mice were housed by groups of 2 to 4 animals per cage and randomized to 7–8 animals per experimental group according to their body weight. No blinding was used during the experiment procedures.

Author Manuscript Author Manuscript Author Manuscript Author Manuscript

Fear Conditioning

Fear conditioning was conducted as described previously[38], using chambers placed in sound-attenuating boxes (635×420×445mm) (Med Associates, USA). Each chamber is equipped with light (infra-red and visible), speakers, and the floor of the chamber consists of a stainless-steel grid connected to a shock generator. A computer running MED PC-IV (Med Associates, USA) controls the presentation of the stimuli (tone and shock). A video camera connected to the MED-VFC-NIR-M automated video-tracking system is used to detect and record movements and freezing behaviour. On the first day (conditioning session), mice were habituated to the testing chamber for 2min followed by the presentation of an auditory cue for 30sec [5kHz tone; 80dB, conditioned stimulus (CS)], co-terminating with a foot shock during the last 2 seconds [0.7mA; unconditioned stimulus (US)]. Mice received four CS-US pairings with an inter-trial interval of 2min. The last CS-US pairing was followed by a 2min-resting phase before mice were returned to their home cage. The entire conditioning session lasted 12min. On the second day, the mouse is re-exposed to the same context with no tone and the freezing response is monitored. Fear was assessed by measuring the percentage of time spent freezing, characterized by a crouching posture and an absence of any visible movement except breathing.

Ethical approval

All experiments were performed in compliance with all relevant ethical regulations. The experiments with postmortem human samples were authorized by the Michigan State University (MSU) Human Research Protection Program. Informed consent for brain autopsies of Rush Religious Orders Study participants was authorized by the Rush University Medical Center Institutional Review Board. The experiments with the 3xTg mice were authorized by the MSU Institutional Review Board and Institutional Animal Care and Use Committee. The experiments with *APP/PSEN1* mice were authorized by the local animal experimentation committee of the Canton de Vaud under license 3207. The committee that approved the license is the Commission cantonale pour l'expérimentation animale.

Human brain samples

Superior temporal cortex (Brodmann area 22) samples were obtained postmortem from participants in the Religious Orders Study who died with an antemortem clinical diagnosis of no cognitive impairment (NCI), mild cognitive impairment (MCI), or AD (n = 8/group) (Supplementary Table 6). Neuropsychological and clinical examinations, as well as postmortem diagnostic evaluations, have been described elsewhere[46]. Demographic, antemortem cognitive testing, and postmortem diagnostic variables were compared among the groups using the nonparametric Kruskal-Wallis Test with Bonferroni correction for multiple comparisons. Gender and apoE ε4 allele distribution were compared using Fisher's Exact Test with Bonferroni correction.

Bioinformatics analysis

For the *in silico* analysis of human brain expression datasets, we have used two sets of publicly available RNA-seq data: (1) from the Harvard Brain Tissue Resource Center

Author Manuscript Author Manuscript Author Manuscript Author Manuscript

(HBTRC), for human primary visual cortex (GN Accession: GN327) and human prefrontal cortex (GN Accession: GN328), and (2) from the Translational Genomics Research Institute, for the whole brain (GN Accession: GN314)[47]. These two datasets are publicly available on GeneNetwork (www.genenetwork.org). For correlation analysis, Pearson's r genetic correlation of the UPR^{mt}, mitophagy, ER stress and HSR gene sets was performed to establish the correlation between these pathways and genes that are associated or are causal to the development of AD. Analyses were performed using the hallmarks and canonical pathways gene sets databases. Additional information about the data sets employed are provided in Supplementary information.

Gene expression analyses

C. elegans—A total of ≈3000 worms per condition, divided in 3 biological replicates, was recovered in M9 buffer from NGM plates and lysed in the TriPure RNA reagent. Each experiment was repeated twice. Total RNA was transcribed to cDNA using QuantiTect Reverse Transcription Kit (Qiagen). Expression of selected genes was analyzed using the LightCycler480 system (Roche) and LightCycler® 480 SYBR Green I Master reagent (Roche). For *C. elegans*, 2 housekeeping genes were used to normalize the expression data, namely actin (*act-1*) and peroxisomal membrane protein 3 (*pmp-3*). See Supplementary Table 7 for the primer list.

Mouse—Total RNA was extracted from tissues using TriPure RNA isolation reagent (Roche) according to the product manual. Expression of selected genes was analyzed using the LightCycler480 system (Roche) and LightCycler® 480 SYBR Green I Master reagent (Roche). The beta-2-Microglobulin *B2m* gene was used as housekeeping reference. See Supplementary Table 8 for the primer list.

Human—Total RNA was extracted using guanidine-isothiocyanate lysis (PureLink, Ambion, Waltham, MA) from cortex samples, and RNA integrity and concentration was verified using Bioanalysis (Agilent, Santa Clara, CA). Samples were randomized based on diagnostic group and assayed in triplicate on a real-time PCR cycler (ABI 7500, Applied Biosystems, Foster City) in 96-well optical plates. qPCR was performed using Taqman hydrolysis probe primer sets (Applied Biosystems) specific for the following human transcripts (Supplementary Table 10): *HSPA9*, *HSPD1*, *YME1L1*, *DNM1L*, *BECN1*, *SQSTM1*, *PARK2*, *COX5A*, *CYC1*. A primer set specific for human *GAPDH* was used as a control housekeeping transcript. For the APP_{Swe}-expressing SH-SY5Y cell line, total RNA was extracted from tissues using TriPure RNA isolation reagent, and expression of selected transcripts was analyzed using the LightCycler480 system (Roche) and LightCycler® 480 SYBR Green I Master reagent (Roche). The *GAPDH* gene was used as housekeeping reference. See Supplementary Table 9 for the primer list. The ddCT method was employed to determine relative levels of each amplicon. Variance component analyses revealed relatively low levels of within-case variability, and the average value of the triplicate qPCR products from each case was used in subsequent analyses.

Author Manuscript Author Manuscript Author Manuscript Author Manuscript

C. elegans strains and plasmids generation, and RNAi experiments

C. elegans strains (Supplementary Table 12) were cultured at 20°C on nematode growth media (NGM) agar plates seeded with *E. coli* strain OP50 unless stated otherwise. Strains used in this study were the wild-type Bristol N2, GMC101 [unc-54p::A-beta-1-42::unc-54 3′-UTR + mtl-2p::GFP][15], CL2122 [(pPD30.38) unc-54(vector) + (pCL26) mtl-2::GFP][48], CB4876 (*clk-1(e2519)*) and MQ1333 (*nuo-6(qm200)*). Strains were provided by the Caenorhabditis Genetics Center (University of Minnesota). The strain CL2122 was outcrossed 3 times in the N2 background, and subsequently used in the control experisments reported herein. AUW9 and AUW10: [GMC101+epfEx6[*atfs-1p::atfs-1]],* and AUW11: *[CL2122+epfEx7[atfs-1p::atfs-1]]* overexpression strains, and AUW12: [*GMC101+clk-1(e2519*) III], AUW13: [*GMC101+nuo-6(qm200)* I] were generated within this study.

Cloning and sequencing primers used in *C. elegans* are listed Supplementary Table 13*. atfs-1p::atfs-1* expression vector was created by amplifying 1488 bp sequence upstream from the transcription start site of *atfs-1* coding region by using worm genomic DNA for the promoter region. The PCR product was digested with PciI and AgeI and ligated into the *pPD30.38* expression vector containing *gfp* coding sequence cloned between inserted AgeI and NotI restriction sites. The *atfs-1* coding sequence (CDS) was instead amplified using using *C. elegans* cDNA, and the PCR product was inserted into *pPD30.38* downstream of the promoter region, between AgeI and NheI restriction sites. The correctness of the *atfs-1p::atfs-1* construct was assessed by sequencing with the indicated *pPD30.38* and *atfs-1 seq*. primers. Two independent GMC101 lines (AUW9 and AUW10), and one CL2122 strain (AUW11) carrying *atfs-1p::atfs-1* transgene as extrachromosomal array were analyzed in the study. Injection marker *myo-2p::gfp* was cloned by amplifying 1179 bp sequence upstream from the transcription start site of *myo-2* coding region by using *C. elegans* genomic DNA. The PCR product was digested with PciI and AgeI and ligated into the *pPD30.38* expression vector containing *atfs-1::gfp* to replace *atfs-1* promoter sequence between PciI and AgeI restriction sites. All transgenic strains were created by using microinjection. For the generation of the GMC101 lines AUW12 and AUW13, GMC101 males were generated after exposure of L4 worms to 30°C for 3h, and let mate with L4 from *clk-1* or *nuo-6* mutant strains. The derived progeny was selected for homozygosis of the GMC101 intestinal GFP marker for few generations, and the homozygosis of the *clk-1* or *nuo-6* mutant alleles verified by amplifying and sequencing a 500 bp region of the worms genomic DNA encompassing the desired mutation (Supplementary Table 13). Bacterial feeding RNAi experiments were carried out as described[49]. Clones used were *atfs-1* (ZC376.7), *ubl-5* (F46F11.4), *mrps-5* (E02A10.1), *dct-1* (C14F5.1), *daf-16* (R13H8.1), *sir-2.1* (R11A8.4), *xbp-1* (R74.3) and *hsf-1* (Y53C10A.12). Clones were purchased from GeneService and verified by sequencing. The novel *atfs-1* RNAi construct (*atfs-1* #2) used in this study was generated by amplifying 1400 bp of the *atfs-1* genomic DNA sequence, starting from the last exon of *atfs-1*. Gateway cloning (Thermo Scientfic) was used to insert the PCR product into the gateway vector pL4440gtwy (Addgene #11344), and verified by sequencing. *atfs-1* knockdown was verified by qPCR for all the *atfs-1* RNAi constructs used herein. For phenotypic studies (see below), worms at the L4 larval stage were allowed to reach adulthood and lay eggs on the treatment plates. The deriving F1 worms were shifted from

Author Manuscript Author Manuscript Author Manuscript Author Manuscript

20°C to 25°C at the L4 stage to induce amyloid accumulation and paralysis, and phenotypes assessed over time as indicated. For double RNAi experiments, we used a combination of *atfs-1* with *mrps-5* RNAi constructs as indicated in the text, with 80% amount of *atfs-1* and 20% *mrps-5* RNAi. For mRNA analysis, synchronized L1 worms were exposed to the treatment plates, and shifted from 20°C to 25°C when reaching the L4 stage. After 24 hours incubation at 25°C, corresponding to day 1 of adulthood, they were harvested in M9 for analysis.

Pharmacological treatment of C. elegans

Doxycycline was obtained from Sigma-Aldrich and dissolved in water[23]. For experiments, a final concentration of 15 μg/mL was used. Olaparib (AZD2281) was dissolved in DMSO to experimental concentrations of 300 nM[34]. Nicotinamide Riboside triflate (NR) was custom synthesized by Novalix (http://www.novalix-pharma.com/) and dissolved in water, and used at a final concentration of 1mM[34]. Compounds were added just before pouring the plates. For phenotyping experiments, parental F0 L4 worms were allowed to reach adulthood and lay eggs on the treatment plates. The deriving F1 worms were therefore exposed to compounds during the full life from eggs until death. For RNA analysis experiments, synchronized L1 worms were exposed to the compounds until harvest. To ensure a permanent exposure to the compound, plates were changed twice a week.

Worm phenotypic assays

Mobility—*C. elegans* movement analysis was performed as described[16], starting from day 1 of adulthood, using the Movement Tracker software. The experiments were repeated at least twice.

Development—50 adult worms per condition were transferred on NGM agar plates (10 worms per plate) and allowed to lay eggs for 3 h. Then they were removed and the number of eggs per plate was counted. 72 h later, the number of L1–L3 larvae, L4 and adult worms was counted. The experiment was done twice with five individual plates.

Paralysis and death score—5 L4 worms per condition were allowed to reach adulthood and lay eggs on the treatment plates. 45 to 60 deriving F1 worms per condition were manually scored for paralysis after poking, as already described[15]. Worms that were unable to respond to any, repeated stimulation, were scored as dead. Results are representative of the data obtained in at least three independent experiments.

Oxygen-consumption assays—Oxygen consumption was measured using the Seahorse XF96 equipment (Seahorse Bioscience)[34,50]. Respiration rates were normalized to the number of worms in each individual well and calculated as averaged values of 5 to 6 repeated measurements. Each experiment was repeated at least twice.

MitoTracker® Orange CMTMRos staining—A population of 20 worms at L4 stage were transferred on plates containing MitoTracker® Orange CMTMRos (Thermo Scientific) at a final concentration of 2ug/uL. The plates were incubated at 25°C and the worms were collected and washed in 200uL of M9 in order to remove the residual bacteria after 24h of

Author Manuscript Author Manuscript Author Manuscript Author Manuscript

treatment. The worms were then incubated for 30 minutes on regular NGM plates at 25°C and mounted on an agar pad in M9 buffer for visualization. Mitochondria were observed by using confocal laser microscopy.

Phalloidin and DAPI staining—A population of 100 L4 worms was incubated for 24h at 25°C. The worms were then washed in M9 and frozen in liquid nitrogen, immediately after they were lyophilized using a centrifugal evaporator. Worms were permeabilized using acetone. 2 U of phalloidin (Thermo Scientific) were resuspended in 20uL of a buffer containing: Na-phosphate pH 7.5 (final concentration 0.2mM), MgCl (final concentration 1mM), SDS (final concentration 0,004%) and dH_2O to volume. The worms were incubated for 1h in the dark and then washed 2 times in PBS and incubated in 20uL of 2ug/mL DAPI in PBS for 5 minutes. Following the immobilization, worms were observed by using confocal laser microscopy.

Quantitative real-time PCR for mtDNA/nuDNA ratio

Absolute quantification of the mtDNA copy number in worms was performed by real-time PCR. Relative values for *nd-1* and *act-3* were compared within each sample to generate a ratio representing the relative level of mtDNA per nuclear genome. The results obtained were confirmed with a second mitochondrial gene *MTCE.26*. The average of at least three technical repeats was used for each biological data point. Each experiment was performed at least on five independent biological samples.

Cell culture and treatments

The SH-SY5Y neuroblastoma cell line expressing the APP Swedish K670N/M671L double mutation (APP_{Swe})[25] was a kind gift of Prof. Cedazo-Minguez (Karolinska Institute, Sweden). Cells were grown in DMEM/F-12, supplemented with 10% fetal bovine serum (FBS, Gibco), GlutaMAX (100X, Gibco) and penicillin/streptomycin (1x, Gibco). Cells were selected in 4 μg/mL Geneticin® Selective Antibiotic (G418 Sulfate, Sigma) and grown for three generations before experiments with cells plated and passaged at 4×10^3 cells/ml and 60% confluence, respectively. Cells were cultured at 37 °C under a 5% CO_2 atmosphere and tested for mycoplasma using Mycoprobe (#CUL001B, R&D systems) following the manufacturer's instructions. Cells were treated with 10μg/mL dox, NR 1 or 3mM, ISRIB 0.5μM (Sigma), as indicated for 24 hours before cell harvesting or fixation. For the immunostaining, cells were fixed with 1x Formal-Fixx (Thermo Scientific) for 15min. After 15min permeabilization with 0.1% Triton X-100, cells were blocked in PBS supplemented with 5% fetal bovine serum for 1 hour and immunostained overnight, at 4°C, with the anti-β-Amyloid 1-42 (1:100, Millipore AB5078P). The secondary antibody was coupled to the Alexa-488 fluorochrome (Thermo Scientific), and nuclei were stained with DAPI (Invitrogen, D1306). After washing in PBS, cell slides were mounted with Dako mounting medium (Dako, S3023) and examined with a Zeiss LSM 700 confocal microscope (Carl Zeiss MicroImaging) equipped with a Plan-Apochromat 40×/1.3 NA oil immersion objective lens using a 488 nm laser. Laser power was set at the lowest intensity allowing clear visualization of the signal. Imaging settings were maintained with the same parameters for comparison between different experimental conditions.

Author Manuscript Author Manuscript Author Manuscript Author Manuscript

Western blot analysis

C. elegans—Worms were lysed by sonication with RIPA buffer containing protease and phosphatase inhibitors (Roche), and analyzed by SDS–PAGE and western blot. The concentration of extracted protein was determined by using the Bio-Rad Protein Assay. Proteins were detected using the following antibodies: anti-β-actin (Sigma), anti-tubulin (Santa Cruz), atp-5, ucr-1 (Oxphos cocktail, Abcam), anti-β-Amyloid, 1-16 (6E10) (BioLegend). In addition to the housekeeping proteins, loading was monitored by Ponceau Red to ensure a homogeneous loading. Pixel intensity was quantified by using ImageJ software. Each immunoblot experiment was repeated at least twice using 3 biological replicates each containing ≈1000 worms.

Mouse—Frozen cortex tissue samples were lysed by mechanical homogenization with RIPA buffer containing protease and phosphatase inhibitors, and analyzed by SDS–PAGE and western blot. Subsequently, the concentration of extracted protein was determined by using the Bio-Rad Protein Assay. Proteins were detected using the following antibodies: HSP60 (Enzo Life Science), CLPP (Sigma), anti-GAPDH (14C10) (Cell Signaling), LONP1 (Sigma), PINK1 (Novus Biologicals), LC3 A/B (Cell Signaling), SDHB (Oxphos cocktail, Abcam), MTCO1 (Abcam), Ubiquitin (Enzo), P62 (BD Transduction Laboratories), Phopsho P62 (Cell Signaling), VDAC (Abcam). In addition to the housekeeping proteins, loading was monitored by Ponceau Red to ensure a homogeneous loading. Antibody detection reactions for all the immunoblot experiments were developed by enhanced chemiluminescence (Advansta) and imaged using the c300 imaging system (Azure Biosystems). Pixel intensity was quantified by using ImageJ software.

Human—Frozen cortex tissue samples were prepared as previously described[51]. Samples were randomized based on diagnostic group and assayed in triplicate. For CLPP, blots were incubated overnight at 4°C with a mouse monoclonal antibody to CLPP (1:1000; clone 2E1D9, ProteinTech) and then incubated for one hour with near-infrared-labeled goat anti-mouse IgG secondary antiserum (IRDye 800LT, 1:10,000; Licor) and analyzed on an Odyssey imaging system (Licor). Following imaging, the membranes were stripped and re-probed with a mouse monoclonal GAPDH antibody (1:10’000; clone 2D9, Origene) overnight followed by 1-hour incubation with near-infrared-labeled goat anti-mouse IgG secondary antiserum and Odyssey imaging. For mtDnaJ/Tid1, blots were incubated overnight at 4°C with both a mouse monoclonal antibody to mtDnaJ/Tid1 (1:500; clone RS13, Cell Signaling) and the GAPDH antibody, followed by goat anti-mouse IgG incubation and Odyssey imaging. Signals for CLPP and mtDnaJ were normalized to GAPDH for quantitative analysis. Details about all the antibodies used are listed in Supplementary Table 11.

Citrate synthase activity assay

Citrate synthase (CS) enzymatic activity was determined in mouse cortex samples and *C. elegans* using the CS assay kit (Sigma). Absorbance at 412 nm was recorded on a Victor X4 (PerkinElmer) with 10 readings over the 1.5 min timespan. These readings were in the linear range of enzymatic activity. The difference between baseline and oxaloacetate-treated samples was obtained and used to calculate total citrate synthase activity according to the

Author Manuscript Author Manuscript Author Manuscript Author Manuscript

formula provided in the manual. The obtained values were normalized by the amount of protein used for each sample.

Extraction of the mitochondrial fraction

Cortexes were placed in a homogenizer glass-Teflon potter tubes with 5ml of a buffer prepared adding 10 ml of 0.1MTris–MOPS and 1 ml of EGTA/Tris to 20 ml of 1M sucrose and bringing the volume to 100ml with distilled water. Homogenization was performed at 1600rpm for 5 minutes. The samples were then centrifuged for 10min at 600g and the supernatants were collected. A second centrifugation at the speed of 7000g for 10 min was performed on the supernatants in order to precipitate the mitochondrial fraction. All the steps were performed on ice or at 4°C.

Histology

Brains hemispheres were harvested from anaesthetized mice and immediately frozen in isopentane. 8-μm cryosections were collected and fixed with 4% paraformaldehyde. For immunostainings, sections were stained with 0,01% Thioflavin S (Sigma) for 15min at room temperature, and after washes in ethanol and PBS, stained with Hoechst (Life Technology). After washing in PBS, tissue sections were mounted with Dako mounting medium. Images were acquired using Leica DM 5500 (Leica Microsystems) CMOS camera 2900 Color at the same exposure time. Quantitative analysis of the immunofluorescence data was carried out by histogram analysis of the fluorescence intensity at each pixel across the images using Image J (Fiji; National Institutes of Health). Appropriate thresholding was employed to all the images of each single experiment to eliminate background signal in the images before histogram analysis. Fluorescence intensity and signal positive areas were calculated using the integrated “analyse particles” tool of the Fiji software, and statistical analysis were performed using Prism 6 (GraphPad Software).

Statistical analyses

Differences between two groups were assessed using two-tailed *t* tests. Differences between more than two groups were assessed by using two-way ANOVA..GraphPad Prism 6 (GraphPad Software, Inc.) was used for all statistical analyses. Variability in all plots and graphs is represented as the s.e.m. All P values < 0.05 were considered to be significant. $*P < 0.05$; $**P \leq 0.01$; $***P \leq 0.001$; $****P \leq 0.0001$ instead stated otherwise. All mouse experiments were performed once. Animals that showed signs of severity, predefined by the animal authorizations were euthanized. These animals, together with those who died spontaneously during the experiments, were excluded from the calculations. These criteria were established before starting the experiments. For motility, fitness and death scoring experiments in *C. elegans*, sample size was estimated based on the known variability of the assay. All experiments were done non-blinded and repeated at least twice.

Data availability

All data generated or analysed during this study are included in this published article (and its supplementary information files). Source data for uncropped gels and for all the individual p values presented herein are provided with the paper. The expression datasets that support the

findings of this study are available in GeneNetwork (www.genenetwork.org) with the identifiers GN327, GN328, GN314[47], and on the Geo Dabatabase (https://www.ncbi.nlm.nih.gov/geo/) with the identifiers (GSE3112, GSE39454)[52,53]. The worm strains generated in this study are available upon request.

Extended Data

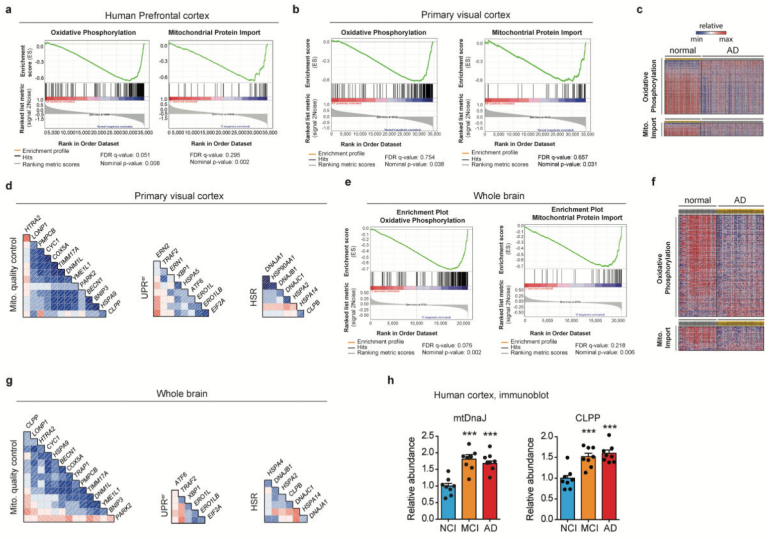

Extended Data Figure 1. Mitochondrial function pathways are perturbed in AD

a, GSEA of Oxphos (FDR:0.051, nominal-*P*=0.008) and mitochondrial import (FDR:0.295, nominal-*P*=0.002) genes in human AD prefrontal cortex (GN328; normal, *n*=195; AD, *n*=388 individuals). **b–g,** GSEA of Oxphos (FDR:0.754, *P*=0.038) and mitochondrial import (FDR:0.657, *P*=0.031) genes in human Alzheimer visual cortex (GN327, *n*=195 normal and *n*=388 AD individuals) (**b**) and whole brain (GN314, *n*=16 normal and 33 AD individuals) (FDR:0.076, *P*=0.002 for Oxphos, FDR:0.218, *P*=0.006 for mitochondrial import) (**e**). Heatmaps of genes from visual cortex (**c**) and whole brain (**f**) datasets. Correlation plots of mitochondrial stress genes, UPR^{er} and HSR levels in human visual cortex (**d**) and whole brain (**g**) from AD patients. For further information, see Supplementary Table 5. **h,** Quantification of immunoblots for mtDNaJ and CLPP (*n*=8 per group) from brains of humans with no cognitive impairment (NCI), mild-cognitive impairment (MCI) and mild/moderate AD. This experiment was performed independently twice. Values in the figure are mean ± s.e.m. ***$P \leq 0.001$. Differences were assessed using two-tailed *t* tests (95% confidence interval). Mito., mitochondrial. For all the individual *p* values, see the Extended Data Fig. 1 Spreadsheet file.

Author Manuscript Author Manuscript Author Manuscript Author Manuscript

Author Manuscript Author Manuscript Author Manuscript Author Manuscript

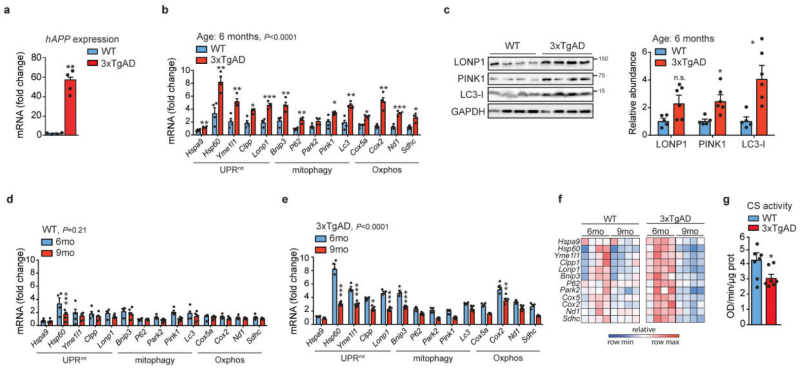

Extended Data Figure 2. MSR analysis and mitochondrial function in 3xTgAD mice

a, Human *APP* expression in cortex tissues of WT and 3xTgAD mice (n=4 animals per group). $^{**}P \leq 0.01$ (P=0.002). **b,** MSR transcript analysis from cortex tissues of WT (n=4 animals) and 3xTgAD mice (n=4 animals) at 6 months of age. **c,** Immunoblot analysis (WT, n=5; 3xTgAD, n=6, WB of 4 representative mice) and quantification of the same samples as in **b**. $^{*}P<0.05$. (P=0.035,0.029). **d–f**, MSR transcript analysis from cortex tissues of WT (**d**, 6mo, n=4 animals; 9mo, n=5 animals) and 3xTgAD mice (**e**, 6mo, n=4 animals; 9mo, n=5 animals) at 6 and 9 months of age, and corresponding heatmaps (**f**) representing relative variation in gene expression between groups. **g,** CS activity assay in cortex tissues from WT and 3xTgAD mice (WT, n=8 animals; 3xTgAD, n=7 animals). $^{*}P<0.05$ (P=0.039). Values in the figure are mean ± s.e.m. $^{*}P<0.05$; $^{**}P \leq 0.01$; $^{***}P \leq 0.001$; n.s., non-significant. Throughout the figure, overall differences between conditions were assessed by two-way ANOVA. Differences for individual genes, proteins or two groups were assessed using two-tailed t tests (95% confidence interval). All experiments were performed independently twice. For uncropped gel source data, see Supplementary Fig. 1. For all the individual p values, see the Extended Data Fig. 2 Spreadsheet file.

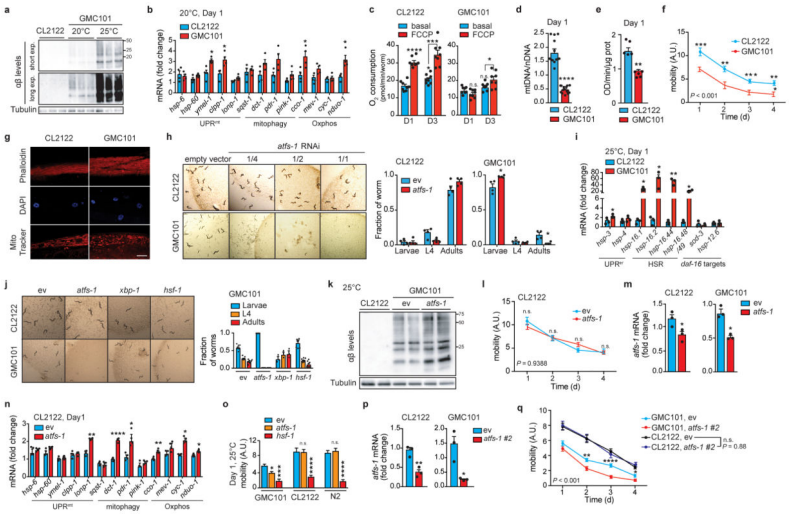

Extended Data Figure 3. Characterization of Aβ proteotoxicity and stress response pathways in GMC101 worms

Author Manuscript Author Manuscript Author Manuscript Author Manuscript

a, Amyloid aggregation in CL2122 and GMC101 worms (*n*=3 biologically independent samples) at 20°C or 25°C. **b,** MSR transcript analysis in worms at 20°C (*n*=3 biologically independent samples). **c,** Respiration assay in CL2122 and GMC101 (CL2122, *n*=8; GMC101, *n*=8 biologically independent samples). **d,** mtDNA/nDNA ratio in CL2122 and GMC101 (*n*=13 animals per group). **e,** CS activity in CL2122 and GMC101 on D1 (*n*=5 biologically independent samples). ***P*≤0.01 (*P*=0.004). **f,** CL2122 and GMC101 mobility (CL2122, *n*=48; GMC101, *n*=59 worms). **g,** Confocal images of D1 adult worms showing muscle cell integrity, nuclear morphology and mitochondrial networks. Scale bar, 10μm. See also **Methods. h**, Representative images and fraction of worms upon *atfs-1* RNAi (*n*=4 independent experiments). **P*<0.05 (Larvae,0.048; Adults,0.035). **i,** Transcript analysis of UPR^{er}, HSR and *daf-16* target genes (*n*=3 biologically independent samples). **j,** Representative images and fraction of worms fed with *atfs-1, xbp-1* and *hsf-1* RNAis at 20°C (*n*=8 per group; *xbp-1*, *n*=3 biologically independent samples). **k**, Amyloid aggregation upon *atfs-1* RNAi (*n*= 2 biological replicates). **l,** Mobility of CL2122 fed with 50% dilution of *atfs-1* RNAi (ev, *n*=48; *atfs-1*$^{1/2}$, *n*=47 worms). **m,** Validation of the *atfs-1* RNAi in CL2122 and GMC101 (*n*=3 biologically independent samples). **n,** MSR transcript analysis of CL2122 upon *atfs-1* RNAi (*n*=3 biologically independent samples). **o,** Mobility of D1 adult worms fed with *atfs-1* or *hsf-1* RNAi at 25°C (CL2122, *n*=22,27,28; GMC101, *n*=27,21,18; N2, *n*=31,38,27 worms). **p**, Validation of the newly generated *atfs-1#2* RNAi (*n*=3 biologically independent samples). For further information, see **Methods. q,** Worm mobility upon *atfs-1#2* RNAi (CL2122, ev, *n*=47; *atfs-1#2*, *n*=42; GMC101, ev, *n*=55; *atfs-1#2*, *n*=46 worms). ev, scrambled RNAi; A.U., arbitrary units. Values in the figure are mean ± s.e.m. **P*<0.05; ***P*≤0.01; ****P*≤0.001; *****P*≤0.0001; n.s., non-significant. Throughout the figure, overall differences between conditions were assessed by two-way ANOVA. Differences for individual genes or two groups were assessed using two-tailed *t* tests (95% confidence interval). All experiments were performed independently at least twice. For uncropped gel source data, see Supplementary Fig. 1. For all the individual *p* values, see the Extended Data Fig. 3 Spreadsheet file.

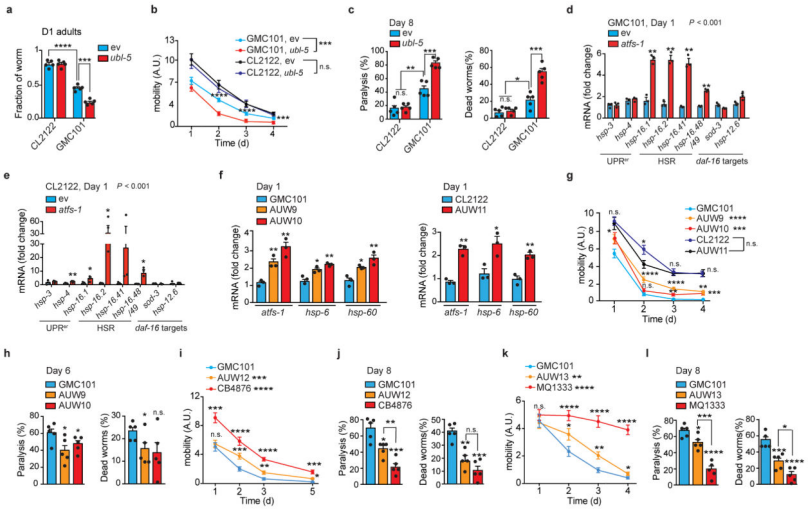

Extended Data Figure 4. Reliance on *ubl-5* and on increased mitochondrial stress response of GMC101 worms

Author Manuscript Author Manuscript Author Manuscript Author Manuscript

a, Fraction of D1 adult worms fed with *ubl-5* RNAi (n=5 biologically independent samples). **b–c,** Mobility of worms (**b**) and percentage of paralyzed and dead D8 adult worms (**c**) upon *ubl-5* RNAi (**b**, CL2122, ev, n=39; *ubl-5*, n=43; GMC101, ev, n=40; *ubl-5*, n=41 worms; n for **c,** 5 biologically independent samples). **d–e,** Transcript analysis of UPR^{er}, HSR and *daf-16* target genes in GMC101 (**d**) and CL2122 (**e**) upon *atfs-1* RNAi (n=3 biologically independent samples) **f,** Validation of the *atfs-1* overexpressing strains AUW9, AUW10 and AUW11 (n=3 biologically independent samples). See also **Methods. g,** Worm mobility in *atfs-1* overexpressing CL2122- and GMC101-derived lines (CL2122, n=40; GMC101, n=57; AUW9, n=40; AUW10, n=38; AUW11, n=42 worms). **h,** Percentage of paralyzed and dead D6 adult worms (n=5biologically independent samples). *P<0.05 (P=0.019,0.046,0.041). **i–j,** Mobility (**i**) and percentage of paralyzed and dead D8 adult (**j**) GMC101, *clk-1* mutants (CB4876), and AUW12 (**i,** GMC101, n= 35; CB4876 n=42; AUW12, n=38 worms; n for **j,** 5 biologically independent samples). **k–l,** Mobility (**k**) and percentage of paralyzed and dead D8 adult (**l**) of GMC101, *nuo-6* mutant (MQ1333), and AUW13 (**k**, GMC101, n=46; MQ1333 n=50; AUW13, n=47 worms; n for **l**, n=5 biologically independent samples). For further information on all these strains, see **Methods** section. ev, scrambled RNAi; A.U., arbitrary units. Values in the figure are mean ± s.e.m. *P<0.05; **P≤0.01; ***P≤0.001; ****P≤0.0001; n.s., non-significant. Throughout the figure, overall differences between conditions were assessed by two-way ANOVA. Differences for individual genes or two groups were assessed using two-tailed t tests (95% confidence interval). All experiments were performed independently at least twice. For uncropped gel source data, see Supplementary Fig. 1. For all the individual p values, see the Extended Data Fig. 4 Spreadsheet file.

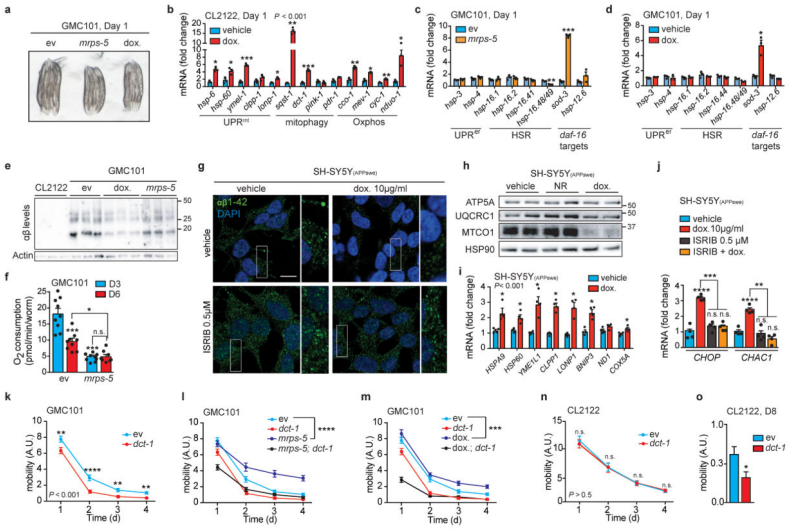

Extended Data Figure 5. Effects of the inhibition of mitochondrial translation and mitophagy in worms, and of compound treatments in mammalian cells

a, Representative images of GMC101 worms upon *mrps-5* RNAi or dox treatment (15μg/mL) from eggs to D1 (n=2 independent experiments). **b,** MSR transcript analysis of dox-treated CL2122 (n=4 biologically independent samples). **c–d,** Transcript analysis of UPR^{er}, HSR and *daf-16* target genes in GMC101 fed with *mrps-5* RNAi (**c**), or treated with

Author Manuscript Author Manuscript Author Manuscript Author Manuscript

dox (15μg/mL) (**d**) (**c–d**, *n*=3 biologically independent samples). **e,** Amyloid aggregation in worms upon *mrps-5* RNAi or dox treatment (*n*=3 biologically independent samples). **f**, Respiration on D3 and 6 in GMC101 fed with *mrps-5* RNAi (*n*=9; *mrps-5* D6, *n*=8 biologically independent samples). **g,** Additional confocal images of the SH-SY5Y$_{(APPSwe)}$ cells stained with the anti-β-Amyloid 1-42 antibody, after dox and ISRIB treatment. Scale bar, 10μm. **h**, Oxphos immunoblot of SH-SY5Y$_{(APPSwe)}$ cells showing the effects of NR (1mM) and dox (10μg/mL) (*n*=2 biologically independent samples). **i–j**, Transcript levels of MSR (**i**) and ATF4 target genes (**j**) in APP$_{Swe}$-expressing cell line after 24h of dox (10μg/mL; *n*=4 biologically independent samples). **k,** Mobility of GMC101 upon *dct-1* RNAi (ev, *n*=54; *dct-1*, *n*=44 worms). **l,** Mobility of GMC101 fed with *dct-1*, *mrsp-5,* or both RNAis (ev, *n*=54; *dct-1*, *n*=44; *mrps-5*, *n*=35; *mrps-5*,*dct-1*, *n*=45 worms). **m,** Mobility of GMC101 treated with dox or fed *dct-1* RNAi (ev, *n* =54; *dct-1*, *n*=44; dox, *n*=52; dox,*dct-1*, *n*=54 worms). **n–o**, Mobility of CL2122 fed with *dct-1* RNAi (**n**) from D1 to 4 (ev, *n*=44; *dct-1*, *n*=40 worms), or (**o**) at D8 (*n*=38 worms, **P*<0.05 (0.018)). ev, scrambled RNAi; dox., doxycycline; NR, nicotinamide riboside; ISRIB, integrated stress response inhibitor; A.U. Values in the figure are mean ± s.e.m. **P*<0.05; ***P*≤0.01; ****P*≤0.001; *****P*≤0.0001; n.s., non-significant. Throughout the figure, overall differences between conditions were assessed by two-way ANOVA. Differences for individual genes or two groups were assessed using two-tailed *t* tests (95% confidence interval). All experiments were performed independently at least twice. For uncropped gel source data, see Supplementary Fig. 1. For all the individual *p* values, see the Extended Data Fig. 5 Spreadsheet file.

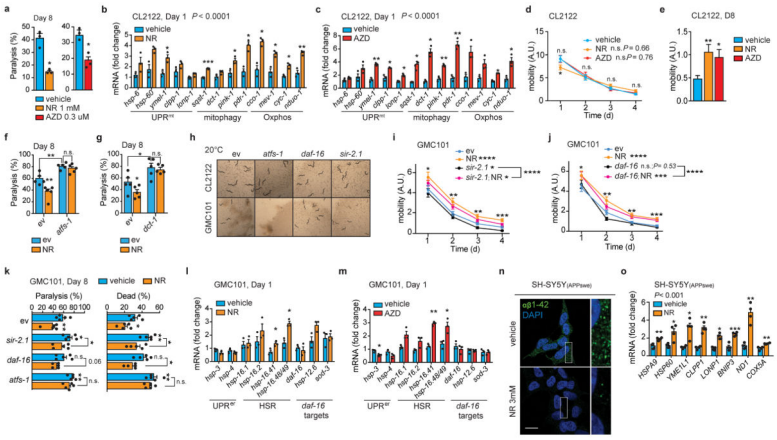

Extended Data Figure 6. Effect of NAD$^+$-boosting compounds and sirtuin depletion in worms, and NR treatment in mammalian cells

a, Percentage of paralyzed D8 adult GMC101 after NR or AZD (*n*=3 independent experiments). **b–c,** MSR transcript analysis of CL2122 treated with NR (**b**,1mM) or AZD (**c**, 0.3μM) (**b–c**, *n*=3 biologically independent samples). **d–e**, Mobility of CL2122 treated with NR (1mM) or AZD (0.3μM) from (**d**) D1 to 4 (vehicle, *n*=44; NR, *n*=48 ; AZD, *n*=43 worms, or (**e**) at D8 (vehicle, *n*=38; NR, *n*=36; AZD, *n*=33 worms, **P*<0.05 (*P*=0.017); ***P*≤0.01 (*P*=0.004)). **f–g**, Percentage of paralyzed D8 adult GMC101 treated with NR upon *atfs-1* RNAi (**f**) or *dct-1* RNAi (**g**) (*n*=5 biologically independent samples). **h,** Representative images of worms fed with *atfs-1*, *sir-2.1*, and *daf-16* RNAis (*n*=2 independent experiments).

Author Manuscript Author Manuscript Author Manuscript Author Manuscript

i, Mobility of NR-treated GMC101 (1mM) fed with *sir-2.1* RNAi (ev, n=52; *sir-2.1,* n=37; NR*,* n=40; *sir-2.1,*NR*,* n=51 worms). **j,** Mobility of NR-treated GMC101 (1mM) fed *daf-16* RNAi (ev, n=52; *daf-16,* n=43; NR*,* n=40; *daf-16,*NR*,* n=48 worms **k**, Percentage of paralyzed and dead D8 adult GMC101 treated with NR or fed *sir-2.1, daf-16* or *atfs-1* RNAis (n=5 biologically independent samples). **l–m,**, Transcript analysis of UPR^{er}, HSR and *daf-16* target genes in GMC101 treated with NR (**l**, 1mM, *P<0.05 (P=0.03,0.008)), or AZD (**m**, 0.3μM, *P<0.05 (P=0.033); **P≤0.01 (P=0.0004) (n=3 biologically independent samples). **n**, Additional confocal images of the intracellular amyloid deposits in the SH-SY5Y$_{(APPSwe)}$ cells after 24 h NR treatment. **o**, Transcript levels of MSR genes in APP_{Swe}-expressing cells after NR (1mM) (n=4 biologically independent samples). NR, nicotinamide riboside; ISRIB, integrated stress response inhibitor; AZD, Olaparib; ev, scrambled RNAi; A.U., arbitrary units. Values in the figure are mean ± s.e.m. *P<0.05; **P≤0.01; ***P≤0.001; ****P≤0.0001; n.s., non-significant. Throughout the figure, overall differences between conditions were assessed by two-way ANOVA. Differences for individual genes or two groups were assessed using two-tailed t tests (95% confidence interval). All experiments were performed independently twice. For all the individual p values, see the Extended Data Fig. 6 Spreadsheet file.

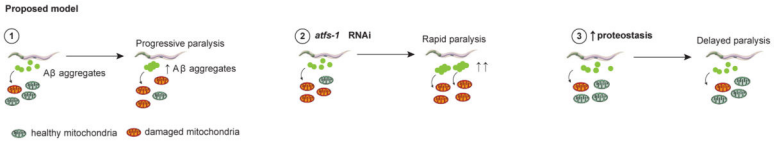

Extended Data Figure 7. Proposed model

Scheme illustrating the role of mitochondrial proteostasis in Aβ proteopathies based on our studies in the GMC101 model. (1) Accumulation of amyloid aggregates triggers mitochondrial dysfunction, which induces the MSR. (2) *atfs-1* depletion results in loss of mitochondrial homeostasis, more pronounced amyloid aggregation and decreased healthspan. (3) Enhancing mitochondrial proteostasis with dox, *mrps-5* RNAi, and NAD^+ boosters (NR and Olaparib), increases organismal fitness, delaying the development of Aβ proteotoxicity.

Supplementary Material

Refer to Web version on PubMed Central for supplementary material.

Acknowledgments

We thank P. Gönczy and M. Pierron (EPFL) for sharing reagents, the *Caenorhabditis* Genetics Center, which is funded by NIH Office of Research Infrastructure Programs (P40 OD010440), for providing worm strains. V.S. is supported by the 'EPFL Fellows' program co-funded by Marie Skłodowska-Curie, Horizon 2020 Grant agreement (665667). D.D. is supported by a fellowship funded by Associazione Italiana per la Ricerca sul Cancro (AIRC) and Marie Curie Actions. S.E.C. is supported by NIH grants (P01AG014449, R21AG053581 and P30 AG053760). This research is supported by the EPFL, NIH (R01AG043930), Systems X (SySX.ch 2013/153), Velux Stiftung (1019), and the Swiss National Science Foundation (31003A-140780).

Author Manuscript Author Manuscript Author Manuscript Author Manuscript

References for main text

1. Alzheimer's A. 2016 Alzheimer's disease facts and figures. Alzheimer's & dementia : the journal of the Alzheimer's Association. 2016; 12:459–509.
2. Dember LM. Amyloidosis-associated kidney disease. Journal of the American Society of Nephrology : JASN. 2006; 17:3458–3471. [PubMed: 17093068]
3. Askanas V, Engel WK. Sporadic inclusion-body myositis: conformational multifactorial ageing-related degenerative muscle disease associated with proteasomal and lysosomal inhibition, endoplasmic reticulum stress, and accumulation of amyloid-beta42 oligomers and phosphorylated tau. Presse medicale. 2011; 40:e219–235.
4. Gauthier S, et al. Why has therapy development for dementia failed in the last two decades? Alzheimer's & dementia : the journal of the Alzheimer's Association. 2016; 12:60–64.
5. Soejitno A, Tjan A, Purwata TE. Alzheimer's Disease: Lessons Learned from Amyloidocentric Clinical Trials. CNS drugs. 2015; 29:487–502. [PubMed: 26187557]
6. Herrup K, et al. Beyond amyloid: getting real about nonamyloid targets in Alzheimer's disease. Alzheimer's & dementia : the journal of the Alzheimer's Association. 2013; 9:452–458. e451.
7. Selfridge JE, EL, Lu J, Swerdlow RH. Role of mitochondrial homeostasis and dynamics in Alzheimer's disease. Neurobiology of disease. 2013; 51:3–12. [PubMed: 22266017]
8. Pellegrino MW, Haynes CM. Mitophagy and the mitochondrial unfolded protein response in neurodegeneration and bacterial infection. BMC biology. 2015; 13:22. [PubMed: 25857750]
9. Beck JS, Mufson EJ, Counts SE. Evidence for Mitochondrial UPR Gene Activation in Familial and Sporadic Alzheimer's Disease. Current Alzheimer research. 2016; 13:610–614. [PubMed: 26687188]
10. Mufson EJ, et al. Mild cognitive impairment: pathology and mechanisms. Acta neuropathologica. 2012; 123:13–30. [PubMed: 22101321]
11. Oddo S, et al. Triple-transgenic model of Alzheimer's disease with plaques and tangles: intracellular Abeta and synaptic dysfunction. Neuron. 2003; 39:409–421. [PubMed: 12895417]
12. Jovaisaite V, Mouchiroud L, Auwerx J. The mitochondrial unfolded protein response, a conserved stress response pathway with implications in health and disease. The Journal of experimental biology. 2014; 217:137–143. [PubMed: 24353213]
13. Cohen E, Bieschke J, Perciavalle RM, Kelly JW, Dillin A. Opposing activities protect against age-onset proteotoxicity. Science. 2006; 313:1604–1610. [PubMed: 16902091]
14. Link CD. C. elegans models of age-associated neurodegenerative diseases: lessons from transgenic worm models of Alzheimer's disease. Experimental gerontology. 2006; 41:1007–1013. [PubMed: 16930903]
15. McColl G, et al. Utility of an improved model of amyloid-beta (Abeta(1)(-)(4)(2)) toxicity in Caenorhabditis elegans for drug screening for Alzheimer's disease. Mol Neurodegener. 2012; 7:57. [PubMed: 23171715]
16. Mouchiroud L, et al. The Movement Tracker: A Flexible System for Automated Movement Analysis in Invertebrate Model Organisms. Current protocols in neuroscience. 2016; 77:8 37 31–38 37 21. [PubMed: 27696358]
17. Nargund AM, Fiorese CJ, Pellegrino MW, Deng P, Haynes CM. Mitochondrial and nuclear accumulation of the transcription factor ATFS-1 promotes OXPHOS recovery during the UPR(mt). Molecular cell. 2015; 58:123–133. [PubMed: 25773600]
18. Nargund AM, Pellegrino MW, Fiorese CJ, Baker BM, Haynes CM. Mitochondrial import efficiency of ATFS-1 regulates mitochondrial UPR activation. Science. 2012; 337:587–590. [PubMed: 22700657]
19. Prahlad V, Morimoto RI. Integrating the stress response: lessons for neurodegenerative diseases from C. elegans. Trends in cell biology. 2009; 19:52–61. [PubMed: 19112021]
20. Benedetti C, Haynes CM, Yang Y, Harding HP, Ron D. Ubiquitin-like protein 5 positively regulates chaperone gene expression in the mitochondrial unfolded protein response. Genetics. 2006; 174:229–239. [PubMed: 16816413]

Author Manuscript Author Manuscript Author Manuscript Author Manuscript

21. Wong A, Boutis P, Hekimi S. Mutations in the clk-1 gene of Caenorhabditis elegans affect developmental and behavioral timing. Genetics. 1995; 139:1247–1259. [PubMed: 7768437]
22. Yang W, Hekimi S. Two modes of mitochondrial dysfunction lead independently to lifespan extension in Caenorhabditis elegans. Aging cell. 2010; 9:433–447. [PubMed: 20346072]
23. Houtkooper RH, et al. Mitonuclear protein imbalance as a conserved longevity mechanism. Nature. 2013; 497:451–457. [PubMed: 23698443]
24. Moullan N, et al. Tetracyclines Disturb Mitochondrial Function across Eukaryotic Models: A Call for Caution in Biomedical Research. Cell reports. 2015
25. Zheng L, et al. Macroautophagy-generated increase of lysosomal amyloid beta-protein mediates oxidant-induced apoptosis of cultured neuroblastoma cells. Autophagy. 2011; 7:1528–1545. [PubMed: 22108004]
26. Forloni G, Colombo L, Girola L, Tagliavini F, Salmona M. Anti-amyloidogenic activity of tetracyclines: studies in vitro. FEBS letters. 2001; 487:404–407. [PubMed: 11163366]
27. Costa R, Speretta E, Crowther DC, Cardoso I. Testing the therapeutic potential of doxycycline in a Drosophila melanogaster model of Alzheimer disease. The Journal of biological chemistry. 2011; 286:41647–41655. [PubMed: 21998304]
28. Loeb MB, et al. A randomized, controlled trial of doxycycline and rifampin for patients with Alzheimer's disease. Journal of the American Geriatrics Society. 2004; 52:381–387. [PubMed: 14962152]
29. Quiros PM, et al. Multi-omics analysis identifies ATF4 as a key regulator of the mitochondrial stress response in mammals. The Journal of cell biology. 2017; 216:2027–2045. [PubMed: 28566324]
30. Munch C, Harper JW. Mitochondrial unfolded protein response controls matrix pre-RNA processing and translation. Nature. 2016; 534:710–713. [PubMed: 27350246]
31. Bao XR, et al. Mitochondrial dysfunction remodels one-carbon metabolism in human cells. eLife. 2016; 5
32. Sidrauski C, McGeachy AM, Ingolia NT, Walter P. The small molecule ISRIB reverses the effects of eIF2alpha phosphorylation on translation and stress granule assembly. eLife. 2015; 4
33. Palikaras K, Lionaki E, Tavernarakis N. Coordination of mitophagy and mitochondrial biogenesis during ageing in C. elegans. Nature. 2015; 521:525–528. [PubMed: 25896323]
34. Mouchiroud L, et al. The NAD(+)/sirtuin pathway modulates longevity through activation of mitochondrial UPR and FOXO signaling. Cell. 2013; 154:430–441. [PubMed: 23870130]
35. Gariani K, et al. Eliciting the mitochondrial unfolded protein response by nicotinamide adenine dinucleotide repletion reverses fatty liver disease in mice. Hepatology. 2016; 63:1190–1204. [PubMed: 26404765]
36. Zhang H, et al. NAD(+) repletion improves mitochondrial and stem cell function and enhances life span in mice. Science. 2016; 352:1436–1443. [PubMed: 27127236]
37. Fang EF, et al. NAD+ Replenishment Improves Lifespan and Healthspan in Ataxia Telangiectasia Models via Mitophagy and DNA Repair. Cell metabolism. 2016; 24:566–581. [PubMed: 27732836]
38. Corcoran KA, Lu Y, Turner RS, Maren S. Overexpression of hAPPswe impairs rewarded alternation and contextual fear conditioning in a transgenic mouse model of Alzheimer's disease. Learning & memory. 2002; 9:243–252. [PubMed: 12359834]
39. Cenini G, Rub C, Bruderek M, Voos W. Amyloid beta-peptides interfere with mitochondrial preprotein import competence by a coaggregation process. Molecular biology of the cell. 2016; 27:3257–3272. [PubMed: 27630262]
40. Gong B, et al. Nicotinamide riboside restores cognition through an upregulation of proliferator-activated receptor-gamma coactivator 1alpha regulated beta-secretase 1 degradation and mitochondrial gene expression in Alzheimer's mouse models. Neurobiology of aging. 2013; 34:1581–1588. [PubMed: 23312803]
41. Martire S, et al. Bioenergetic Impairment in Animal and Cellular Models of Alzheimer's Disease: PARP-1 Inhibition Rescues Metabolic Dysfunctions. Journal of Alzheimer's disease : JAD. 2016; 54:307–324. [PubMed: 27567805]

Author Manuscript Author Manuscript Author Manuscript Author Manuscript

42. Kim HE, et al. Lipid Biosynthesis Coordinates a Mitochondrial-to-Cytosolic Stress Response. Cell. 2016; 166:1539–1552. e1516. [PubMed: 27610574]
43. Wang X, Chen XJ. A cytosolic network suppressing mitochondria-mediated proteostatic stress and cell death. Nature. 2015; 524:481–484. [PubMed: 26192197]
44. Wrobel L, et al. Mistargeted mitochondrial proteins activate a proteostatic response in the cytosol. Nature. 2015; 524:485–488. [PubMed: 26245374]
45. D'Amico D, Sorrentino V, Auwerx J. Cytosolic Proteostasis Networks of the Mitochondrial Stress Response. Trends in biochemical sciences. 2017
46. Tiernan CT, et al. Protein homeostasis gene dysregulation in pretangle-bearing nucleus basalis neurons during the progression of Alzheimer's disease. Neurobiology of aging. 2016; 42:80–90. [PubMed: 27143424]
47. Liang WS, et al. Alzheimer's disease is associated with reduced expression of energy metabolism genes in posterior cingulate neurons. Proceedings of the National Academy of Sciences of the United States of America. 2008; 105:4441–4446. [PubMed: 18332434]
48. Fonte V, et al. Suppression of in vivo beta-amyloid peptide toxicity by overexpression of the HSP-16.2 small chaperone protein. The Journal of biological chemistry. 2008; 283:784–791. [PubMed: 17993648]
49. Kamath RS, Martinez-Campos M, Zipperlen P, Fraser AG, Ahringer J. Effectiveness of specific RNA-mediated interference through ingested double-stranded RNA in Caenorhabditis elegans. Genome biology. 2001; 2:RESEARCH0002. [PubMed: 11178279]
50. Koopman M, et al. A screening-based platform for the assessment of cellular respiration in Caenorhabditis elegans. Nature protocols. 2016; 11:1798–1816. [PubMed: 27583642]
51. Counts SE, Nadeem M, Lad SP, Wuu J, Mufson EJ. Differential expression of synaptic proteins in the frontal and temporal cortex of elderly subjects with mild cognitive impairment. Journal of neuropathology and experimental neurology. 2006; 65:592–601. [PubMed: 16783169]
52. Greenberg SA, et al. Plasma cells in muscle in inclusion body myositis and polymyositis. Neurology. 2005; 65:1782–1787. [PubMed: 16344523]
53. Zhu W, et al. Genomic signatures characterize leukocyte infiltration in myositis muscles. BMC medical genomics. 2012; 5:53. [PubMed: 23171592]

Author Manuscript Author Manuscript Author Manuscript Author Manuscript

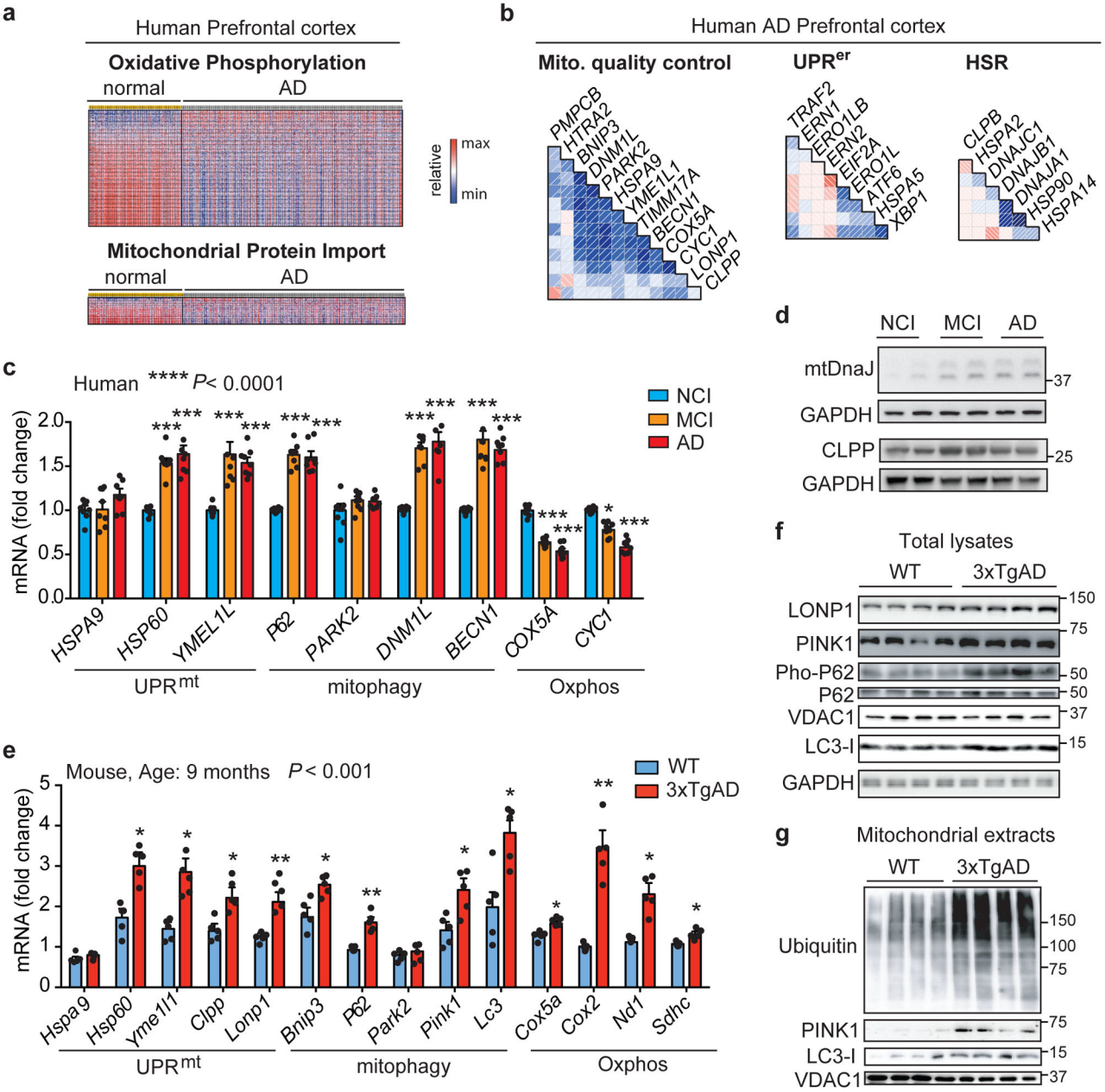

Figure 1. Mitochondrial dysfunction in AD is typified by a conserved Mitochondrial Stress Response

a Heatmap of the expression levels of Oxphos and mitochondrial import genes in human AD prefrontal cortex (GN328; normal, *n*=195; AD, *n*=388 individuals). **b,** Correlation plots of mitochondrial stress genes, UPR^{er} and HSR levels in prefrontal cortex from AD patients (GN328; *n* as in **a**). See Extended Data Fig. 1 and Supplementary Table 1–5. **c–d**, Transcript analysis of the Mitochondrial Stress Response signature (**c**; MSR, *n*=8 per group) and Western blot (**d**, WB, *n*=2 individuals) of mtDNaJ and CLPP in brains of humans with no cognitive impairment (NCI), mild-cognitive impairment (MCI) and mild/moderate AD. **e–f,** Transcript (**e**) and immunoblot (**f**) analysis of MSR genes in cortex of 9-months old wild

Author Manuscript Author Manuscript Author Manuscript Author Manuscript

type (WT) and 3xTgAD mice (WT, n=5; 3xTgAD, n=5 for RNA; WT, n=4; 3xTgAD, n=4 for WB, representative of 6 animals). **g,** Immunoblot (WT, n=4; 3xTgAD, n=4, WB representative of 5 animals) of mitophagy and autophagy proteins in mitochondrial extracts from cortex tissues of the animals in **e–f**. Values in the figure are mean ± s.e.m. *P<0.05; **P≤0.01; ***P≤0.001. Throughout the figure, overall differences between conditions were assessed by two-way ANOVA. Differences for individual genes/proteins were assessed using two-tailed t tests (95% confidence interval). All experiments were performed independently twice. Mito., mitochondrial. See also Extended Data Fig. 2. For uncropped gel source data, see Supplementary Fig. 1. For all the individual p values, see the Fig. 1 Spreadsheet file.

Author Manuscript Author Manuscript Author Manuscript Author Manuscript

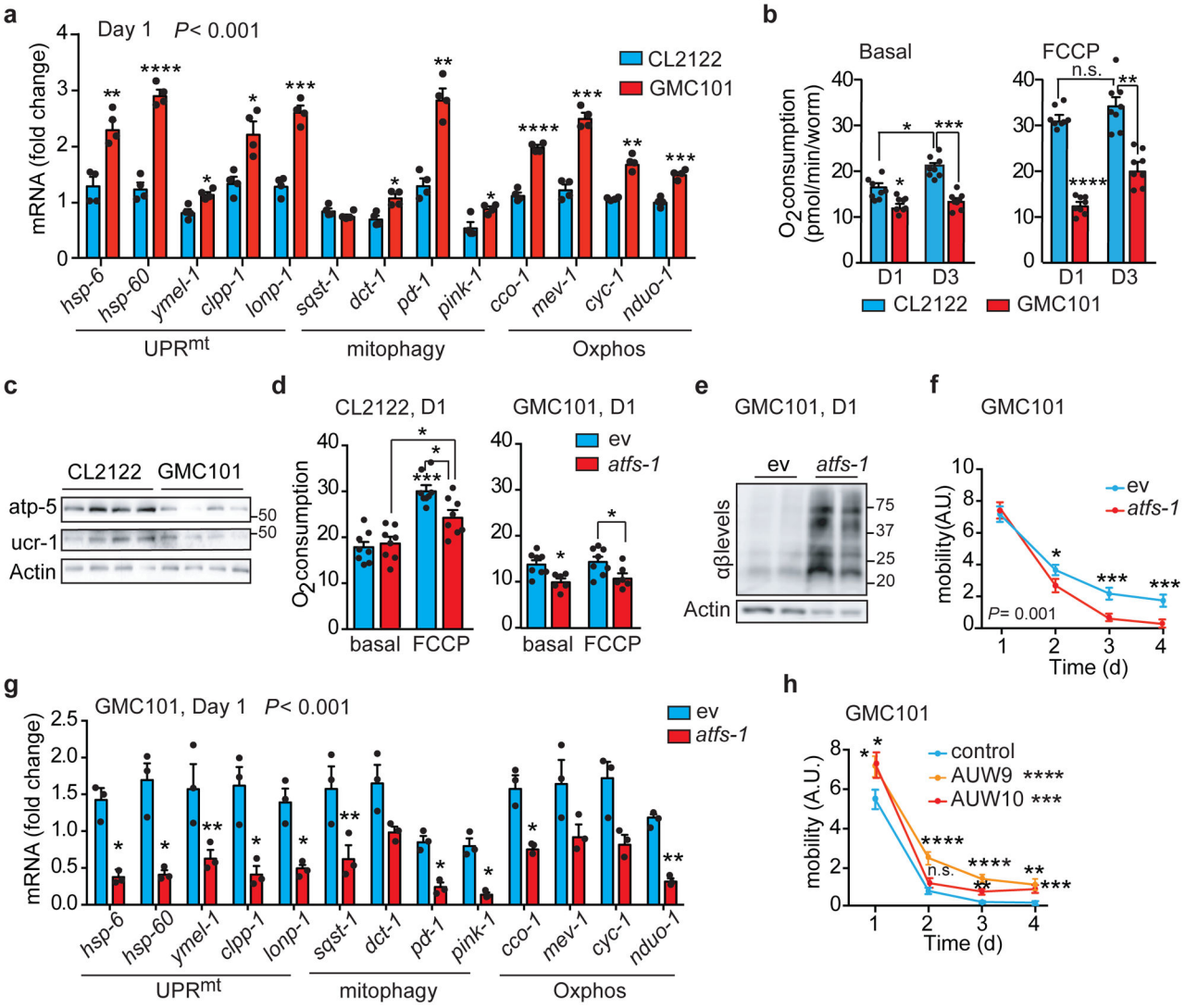

Figure 2. Mitochondrial dysfunction and reliance on *atfs-1* of GMC101 worms upon proteotoxic stress

a, MSR transcript analysis in CL2122 and GMC101 (n=3 biologically independent samples). **b,** Basal respiration and after FCCP (45 min, 10μM) of day 1 (D1) and 3 (D3) adult worms (CL2122, n=8; GMC101, n=8 biologically independent samples). **c,** Immunoblot (CL2122, n=4; GMC101, n=4, WB representative of 5 biological replicates) of Oxphos proteins in control and GMC101 at D1. **d,** Respiration assay as in **b** in CL2122 (ev, n=8; *atfs-1*, n=8 biologically independent samples) and GMC101 (ev, n=8; *atfs-1*, n=6 biologically independent samples) fed with *atfs-1* RNAi. **e,** Amyloid aggregation in GMC101 upon *atfs-1* RNAi shown by WB of 2 biological repeats. **f,** Mobility of GMC101 fed with 50% *atfs-1* RNAi (ev, n=59; *atfs-1*$^{1/2}$, n=50 worms). **g,** MSR transcript analysis of GMC101 upon *atfs-1* RNAi (n=3 biologically independent samples). **h,** Mobility of control and *afts-1* overexpressing GMC101 strains (GMC101, n=61; AUW9, n=48; AUW10, n=41 worms). Values in the figure are mean ± s.e.m. *P<0.05; **P≤0.01; ***P≤0.001; ****P≤0.0001; n.s., non-significant. Throughout the figure, overall differences between

Author Manuscript Author Manuscript Author Manuscript Author Manuscript

conditions were assessed by two-way ANOVA. Differences for individual genes/proteins were assessed using two-tailed *t* tests (95% confidence interval). All experiments were performed at least independently twice. Mito., mitochondrial; ev, scrambled RNAi; A.U., arbitrary units. See also Extended Data Fig. 3–4. For uncropped gel source data, see Supplementary Fig. 1. For all the individual *p* values, see the Fig. 2 Spreadsheet file.

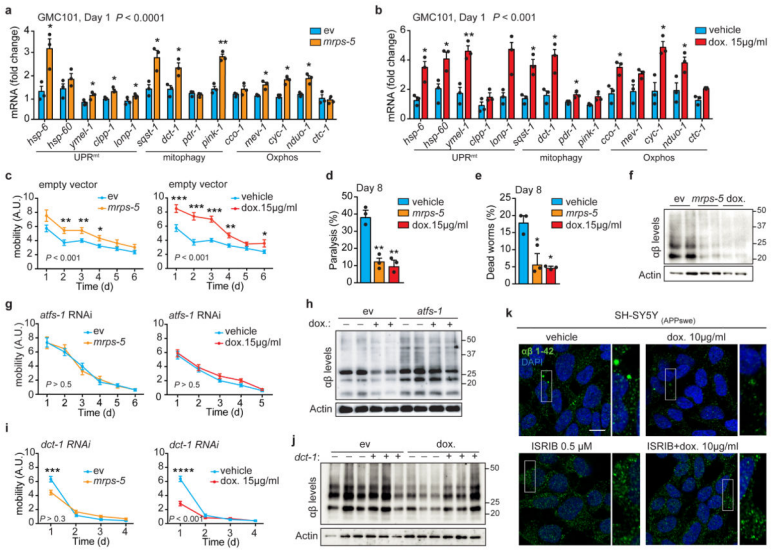

Figure 3. Inhibiting mitochondrial translation reduces Aβ proteotoxicity and aggregation in GMC101 worms and in cells

a–b, MSR transcript levels in GMC101 fed *mrps-5* RNAi or treated with dox (**a** and **b**, *n*=3 biologically independent samples). **c,** Mobility of GMC101 upon *mrps-5* RNAi (*n*=35 worms) or dox treatment (*n*=54 worms). **d–e,** Percentage of paralyzed (**d**) and dead (**e**) D8 adult GMC101 worms after *mrps-5* RNAi or dox treatment (*n*=3 independent experiments). **f,** Western-blot of amyloid aggregation in GMC101 upon *mrps-5* RNAi or dox treatment (*n*=2 biologically independent samples). **g**, Mobility of GMC101 upon *atfs-1* RNAi feeding (ev, *n*=54; *mrps-5*, n=49; dox, n=49 worms). **h,** Amyloid aggregation in dox-treated GMC101 upon *atfs-1* RNAi (*n*=2 biological replicates). **i**, Mobility of GMC101 upon *dct-1* RNAi (ev, n=44; dox, *n*=59; *mrps-5, n*=66 worms). ***$P \leq 0.001$ (P=0.0004); ****$P \leq 0.0001$. **j,** Amyloid aggregation in dox-treated GMC101 upon *dct-1* RNAi (*n*=3 biologically independent samples). **k**, Confocal images of the SH-SY5Y neuroblastoma cell line stained with the anti-β-Amyloid 1-42, after dox and, where indicated, ISRIB treatments for 24 h. Scale bar, 10μm. See **Methods** for further details. Values in the figure are mean ± s.e.m. *$P<0.05$; **$P \leq 0.01$; ***$P \leq 0.001$; ****$P \leq 0.0001$. Throughout the figure, overall differences between conditions were assessed by two-way ANOVA. Differences for individual genes or two groups were assessed using two-tailed *t* tests (95% confidence interval). All experiments were performed independently at least twice. ev, scrambled RNAi; dox., doxycycline; A.U., arbitrary units; ISRIB, integrated stress response inhibitor. See also Extended Data Fig. 5. For uncropped gel source data, see Supplementary Fig. 1. For all the individual *p* values, see the Fig. 3 Spreadsheet file.

Author Manuscript Author Manuscript Author Manuscript Author Manuscript

Author Manuscript Author Manuscript Author Manuscript Author Manuscript

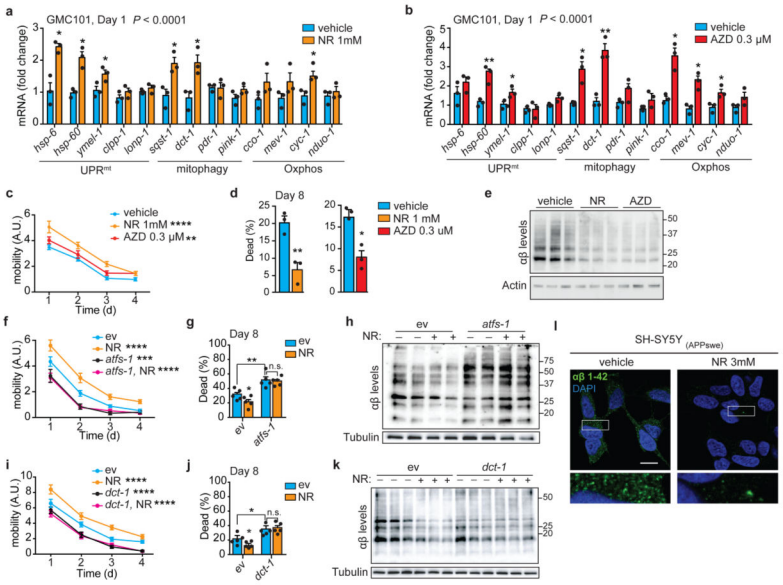

Figure 4. NAD$^+$ boosters reduce Aβ proteotoxicity and aggregation in GMC101 worms and cells

a–b, MSR transcripts in GMC101 worms treated with nicotinamide riboside (**a**, NR) or Olaparib (**b**, AZD). **a–b**, *n*=3 biologically independent samples. **c,** Mobility of GMC101 treated with NR (*n*=50 worms) or AZD (*n*=39 worms). ** *P*≤0.001 (AZD,0.006); **** *P*≤0.0001 (NR). **d,** Percentage of dead D8 adult GMC101 after NR or AZD (*n*=3 independent experiments). **e,** Western-blot of amyloid aggregation in GMC101 after NR or AZD (*n*=3 biologically independent samples for all groups). **f**, Mobility of GMC101 treated with NR upon *atfs-1* RNAi feeding (ev, *n*=52; *atfs-1*, *n*=38; NR, *n*=40; NR, *atfs-1*, *n*=41 worms). *** *P*≤0.001 (*atfs-1*,0.0006). **g,** Percentage of dead D8 adult GMC101 treated with NR upon *atfs-1* RNAi (*n*=5 biologically independent samples). **h,** Amyloid aggregation in NR-treated GMC101 upon *atfs-1* RNAi feeding (WB representative of 2 biological replicates). **i**, Mobility of NR-treated GMC101 upon *dct-1* RNAi (ev, *n*=41; *dct-1*, *n*=40; NR, *n*=39; NR, *dct-1*, *n*=50 worms). **j,** Percentage of dead D8 adult GMC101 treated with NR upon *dct-1* RNAi (*n*=5 biologically independent samples). **k,** Amyloid aggregation immunoblot in NR-treated GMC101 upon *dct-1* RNAi (*n*=3 biologically independent samples). **l**, Confocal images of APP_{Swe} SH-SY5Y cells stained with anti-β-Amyloid 1-42, after 24 h NR treatment. Scale bar, 10μm. Values in the figure are mean ± s.e.m. * *P*<0.05; ** *P*≤0.01; *** *P* ≤ 0.001; **** *P*≤0.0001; n.s., non-significant. Throughout the figure, overall differences between conditions were assessed by two-way ANOVA. Differences for individual genes or two groups were assessed using two-tailed *t* tests (95% confidence interval). All experiments were performed independently at least twice. ev, scrambled RNAi; A.U., arbitrary units. See also Extended Data Fig. 6. For uncropped gel source data, see Supplementary Fig. 1. For all the individual *p* values, see the Fig. 4 Spreadsheet file.

Author Manuscript Author Manuscript Author Manuscript Author Manuscript

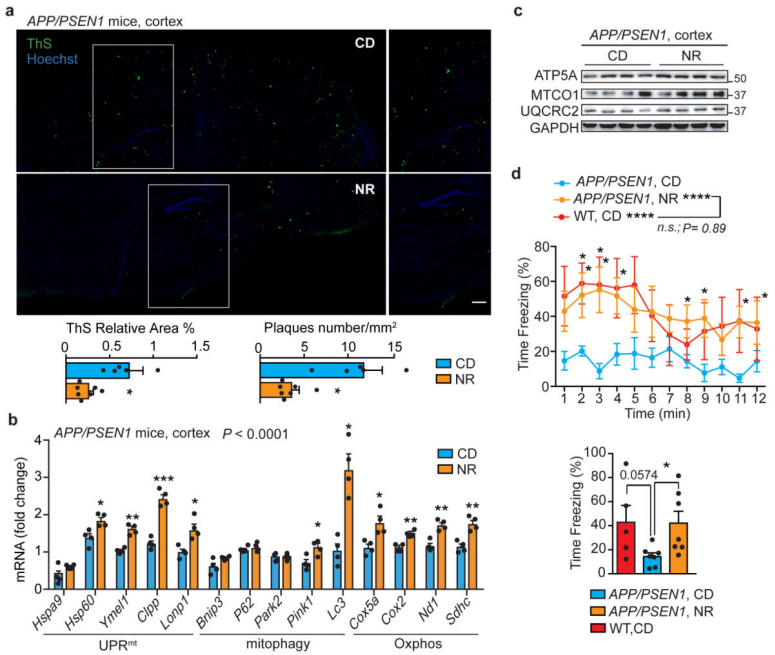

Figure 5. NR reduces Aβ deposits, induces the MSR and improves contextual memory in transgenic AD mice

a, Representative images and corresponding quantification of plaques in cortex samples of *APP/PSEN1* AD mice following NR treatment, stained using Thioflavin S (ThS) (CD, n=5 animals; NR, n=7 animals; NR 400mg/kg/day for 10 weeks). Scale bar, 200μm. *P<0.05 (relative % area,0.041; number,0.014). **b–c,** MSR transcript (**b**) and immunoblot (**c**) analyses of cortex samples of *APP/PSEN1* mice following NR treatment (**b**, n=5 animals per group; **c**, n=4 animals per group). Data in **b**,**c** are representative of two independent experiments. **d**, Contextual fear conditioning in WT (n=5 animals) and *APP/PSEN1* mice with or without NR treatment (n=7 animals), plotted in function of the time intervals (left) or as average of the total obtained values (right). *P<0.05 (P=0.03); ****P≤0.0001. One-tail t test performed between WT and *APP/PSEN1* averaged values (P=0.0574, 95% confidence interval). Values in the figure are mean ± s.e.m. *P<0.05; **P≤0.01; ***P≤0.001; ****P≤0.0001; n.s., non-significant. Throughout the figure, overall differences between conditions were assessed by two-way ANOVA. Differences for individual genes or two groups were assessed using two-tailed t tests (95% confidence interval). See **Methods** for further details. CD, chow diet. For uncropped gel source data, see Supplementary Fig. 1. For all the individual p values, see the Fig. 5 Spreadsheet file.